Available online at www.sciencedirect.com
ScienceDirect
Trans. Nonferrous Met. Soc. China 35(2025) 932−944
Transactions of Nonferrous Metals Society of China
www.tnmsc.cn

High magnetic field-induced structural transformation of $NiFe_2O_4/Fe_2O_3$ heterostructures for enhancing lithium storage performance

Jia-qi LIU[1], Rong-yuan ZHANG[1], Xiao-yang WANG[1],
Jun WANG[2], Tie LIU[3], Wei-bin CUI[3], Qiang WANG[3], Shuang YUAN[1,4,5]

1. School of Metallurgy, Northeastern University, Shenyang 110819, China;
2. State Key Laboratory of Solidification Processing, Northwestern Polytechnical University, Xi'an 710072, China;
3. Key Laboratory of Electromagnetic Processing of Materials (Ministry of Education), Northeastern University, Shenyang 110819, China;
4. Key Laboratory of Ecological Metallurgy of Multimetallic Mineral (Ministry of Education), Northeastern University, Shenyang 110819, China;
5. Engineering Research Center of Frontier Technologies for Low-carbon Steelmaking (Ministry of Education), Shenyang 110819, China

Received 19 July 2023; accepted 29 March 2024

Abstract: In response to the limitations of conventional chemical synthesis methods for the structural modulation of nanomaterials, an innovative high magnetic field-assisted wet chemical synthesis method was proposed to prepare $NiFe_2O_4/Fe_2O_3$ heterostructures. It is found that the high-energy physical field could induce a more homogeneous morphology of $NiFe_2O_4/Fe_2O_3$, accompanied by phase transformation from Fe_2O_3 to $NiFe_2O_4$. As a result, the optimized structure obtained under the magnetic field endows $NiFe_2O_4/Fe_2O_3$ with enhanced performance for the lithium-ion battery anode, as evidenced by an increase of 16% (1200 mA·h/g) in discharge capacity and 24% in ultra-stable cycling performance (capacity retention of 97.1%). These results highlight the feasibility of high magnetic fields in modulating material structure and enhancing lithium storage performance.

Key words: high magnetic field; $NiFe_2O_4/Fe_2O_3$; heterostructure; structural regulation; lithium-ion battery anode

1 Introduction

Lithium-ion batteries (LIBs) have developed into a key foundation for the new energy industry and an essential technology for achieving the goal of "carbon peaking and carbon neutrality" [1−3]. To satisfy the demand for the next-generation high-specific-capacity LIBs in electric vehicles and aerospace, Fe_2O_3 is considered an ideal anode candidate material due to its high theoretical capacity (1007 mA·h/g), low cost, substantial abundance, and rich redox chemistry [4]. Nevertheless, it is also restricted by large volume expansion and low electronic conductivity [5]. One of the effective approaches to improve electronic conductivity is constructing heterogeneous structures by utilizing metal oxides with different energy bands [6−8].

Metal-organic frameworks (MOFs), which are characterized by large specific surface area, adjustable composition, high porosity, and easy functional modification, have become hot precursors for constructing porous and heterogeneous structures in recent years [9,10]. The morphology and the structure of MOFs can greatly affect their

Corresponding author: Shuang YUAN, Tel: +86-24-83681171, E-mail: yuans@smm.neu.edu.cn
DOI: https://doi.org/10.1016/S1003-6326(24)66724-5

electrochemical performance as LIB anodes [11]. Conventional chemical synthesis methods are uncontrollable as they largely depend on environmental factors, such as temperature, humidity, and pH [12,13]. Therefore, it is challenging to adopt an effective way to regulate the synthesis process of MOFs.

High magnetic field (HMF), as an emerging technology, can transfer high-intensity energy contactless to atomic or molecular scales [14,15]. Great efforts have shown that HMF can influence the growth process of materials by magnetizing forces (Lorentz force), magnetization energy (Seeman energy), and magnetic dipole interactions [16−18]. For example, WANG et al [16] modulated the loading of Pt in the Ni_2P/NF catalyst through the magnetohydrodynamic (MHD) effect caused by magnetizing forces. DING et al [17] regulated the crystal phase of MoS_2 and obtained pure-phase 1T-MoS_2 under the influence of magnetic free energy. Thus, it is feasible to modulate the morphology and structure of materials by magnetic fields.

Herein, we developed an advanced magnetic field-assisted wet chemical synthesis strategy to prepare FeNi-based MOF (FeNi-MIL) and then obtained $NiFe_2O_4/Fe_2O_3$ heterostructures (NFO/FO) via pyrolysis. In this study, the role and action mechanism of HMF in the nucleation and growth process of materials were explored, taking the microscopic morphology and physical phase structure as the main entry points. Furthermore, the influence of this magnetic field on the LIB anode performance was also investigated. This work is of guiding significance in external field modulation on the structure and lithium storage properties of nanomaterials.

2 Experimental

2.1 Preparation of materials

FeNi-MIL was synthesized by an adapted solvothermal method as previously reported [19]. Typically, 27 mg $FeCl_3·6H_2O$, 42 mg $Ni(NO_3)_2·6H_2O$, and 16.6 mg 1,4-dicarboxybenzene (1,4-BDC) were dissolved in 12 mL N,N-dimethylformamide (DMF), and magnetically stirred for 1 h at room temperature until they were well mixed. Then, the mixed solution was transferred to a sealed Teflon-lined autoclave and held at 150 °C for 3 h in a thermostat oven. The products obtained in the conventional environment and at a HMF of 6 T were named FeNi-MIL-0 and FeNi-MIL-6, respectively. The HMF-assisted wet chemical synthesis device used therein was developed independently by the Key Laboratory of Electro-magnetic Processing of Materials (Ministry of Education), Northeastern University, China, and the schematic diagram is demonstrated in Fig. 1. The device was composed of a superconducting magnet, a heating system, and a wet chemical reaction system. The magnetic field distribution in the autoclave when magnetic field strength reached 6 T is shown in Fig. 1(c). The maximum difference in the magnetic field strength was about 0.05 T, less than 1% of magnetic field strength. Therefore, it can be assumed that the whole chemical synthesis system was formulated in a uniform magnetic field. In addition, Fe-MIL-6 was prepared by the same method without $Ni(NO_3)_2·6H_2O$ at a magnetic field strength of 6 T as the control group. Eventually, NFO/FO-0, NFO/FO-6, and FO-6 were obtained by the pyrolysis of FeNi-MIL-0, FeNi-MIL-6, and Fe-MIL-6 in air at 600 °C for 4 h with a heating rate of 3 °C/min, respectively.

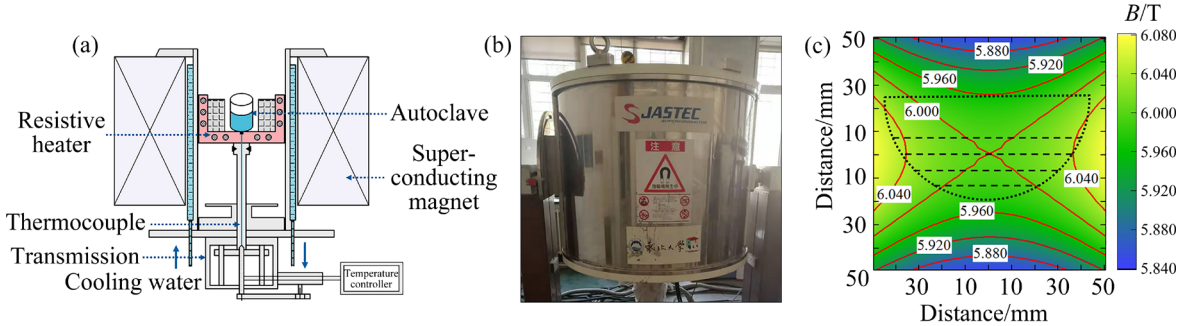

Fig. 1 Schematic diagram (a) and actual photo (b) of electrochemical reaction equipment with HMF, and magnetic field distribution in autoclave (c) (*B* is magnetic field strength)

2.2 Characterization

The microstructures were characterized by scanning electron microscopy (SEM, SU8010) at 5 kV. X-ray diffraction (XRD) patterns were acquired with a Rigaku Ultima IV diffractometer to reveal the phase structure. The Fourier transform-infrared (FT-IR) spectra were collected from the FTIR−8400s spectrometer. The specific surface area and pore distribution were calculated using the Brunauer−Emmett−Teller (BET) method on the Tristar 3000. X-ray photoelectron spectroscopy (XPS) measurement was conducted using a Thermo Scientific K-Alpha instrument with Al K_α radiation to analyze the chemical composition.

2.3 Electrochemical measurement

The electrochemical measurement was performed on the Land battery measurement system and electrochemical workstation (VSP, Bio-Logic). The working electrode was prepared by means of conventional methods, in which the ink containing an active material, acetylene black and poly-vinylidene fluoride (mass ratio of 8:1:1) was uniformly mixed through N-methyl-2-pyrrolidone and coated on copper foil as the anode of LIBs. The coin cell (CR2025) was assembled in high-purity Ar gas without water and oxygen. The cyclic voltammogram (CV) curves were acquired through an electrochemical workstation in a scan range of 0.01−3 mV/s. The charge−discharge curves, cycle stability, and rate performance were evaluated by galvanostatic charge−discharge tests on the Land measurement system.

3 Results and discussion

3.1 Effect of HMF

FeNi-MIL was synthesized using a simple solvothermal method with or without applying a HMF. As shown in Figs. 2(a_1, a_2), FeNi-MIL-0 without applying HMF exhibits a large number of irregular particles as well as a few rod-like structures. In contrast, FeNi-MIL-6 and Fe-MIL-6 obtained in the presence of HMF exhibit a regular spindle structure, with the former being more uniform in shape and size (Figs. 2(b_1, b_2, c_1, c_2)).

The morphological transformation of FeNi-MIL was elucidated by the effect of magnetic field on the solute distribution in solution as well as the nucleation and growth rate of the crystals. FeNi-MIL primary crystals formed without HMF fall into the bottom layer with gravity in the reaction process, with the upper solute gradually consumed. Subsequently, the ongoing nucleation and growth result in the continuous growth of underlying crystals into rod-like structures, while the crystals formed in the later stages exhibit irregular nanoparticles. Under the action of HMF, the MHD effect produces a continuous perturbation to the solution because the charged particles are subjected to the Lorentz force. Consequently, the gravitational effect is attenuated, and FeNi-MIL primary crystals are dispersed in the solution, thus facilitating their uniform growth. Furthermore, the Seeman energy caused by the HMF increases the nucleation rate while reducing the growth rate, which is also an

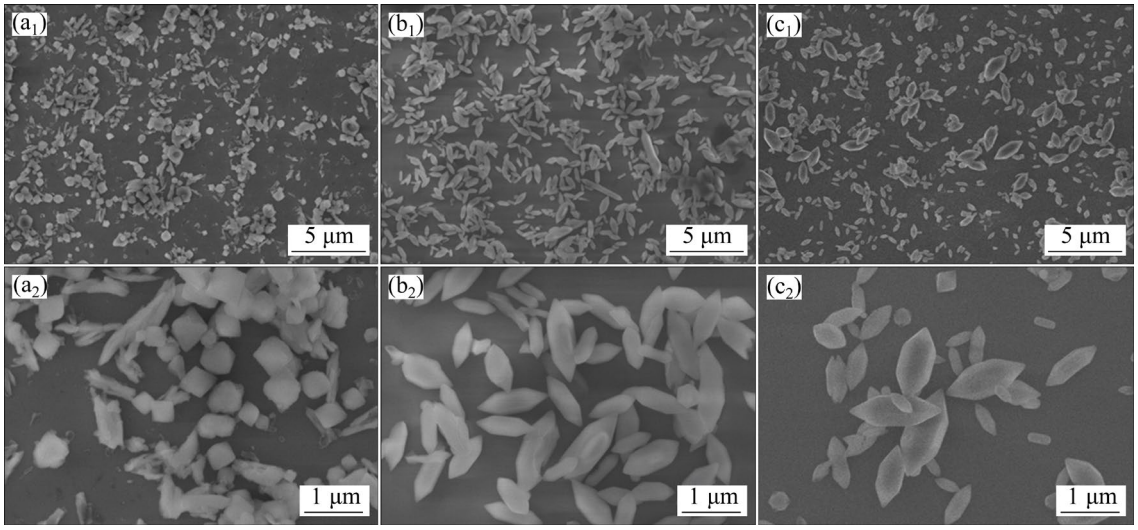

Fig. 2 SEM images of FeNi-MIL-0 (a_1, a_2), FeNi-MIL-6 (b_1, b_2), and Fe-MIL-6 (c_1, c_2)

important factor for the uniform growth of FeNi-MIL-6 [20].

FT-IR spectrum measurement was performed to reveal the functional groups and chemical bonds of the synthesized material. As shown in Fig. 3, the broad peak at 3000−3500 cm^{-1} corresponds to the O—H stretching vibration of water molecules adsorbed from air [21]. The peaks at 1662, 1598, and 1383 cm^{-1} are ascribed to the stretching vibration of O—C═O as well as asymmetric and symmetric vibrations of the dicarboxylate linker [22].

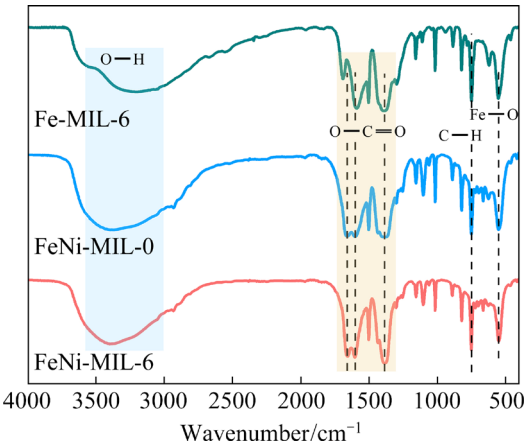

Fig. 3 FT-IR spectra of Fe-MIL-6, FeNi-MIL-0, and FeNi-MIL-6

Besides, the peak of C—H bending vibration appears at 752 cm^{-1}, belonging to the aromatic ring in the terephthalic acid linker [23]. There is a visible peak of the Fe—O stretching vibration at 548 cm^{-1}, indicating the coupling between iron ions and the carboxylic group of terephthalate linkers [24]. All the above results indicate the successful synthesis of FeNi-MIL. More importantly, all the absorption peaks of FeNi-MIL-6 and FeNi-MIL-0 can be well matched, indicating that the HMF only acts on the morphology of FeNi-MIL, rather than on its crystal structure.

3.2 Structural characteristics

The NFO/FO-0, NFO/FO-6, and FO-6 were prepared by the pyrolysis of FeNi-MIL-0, FeNi-MIL-6, and Fe-MIL-6 in air, respectively. In terms of NFO/FO-0, small irregular particles migrate and reunify into large agglomerates in the pyrolysis process (Fig. 4(a)), which buries internal active sites and harms the insertion and detachment of lithium ions. However, for NFO/FO-6 and FO-6, the spindles obtained in the presence of HMF evolve into a homogeneous and regular porous “shuttle” structure in the pyrolysis process, as shown in Figs. 4(b) and (c). The abundant pores are

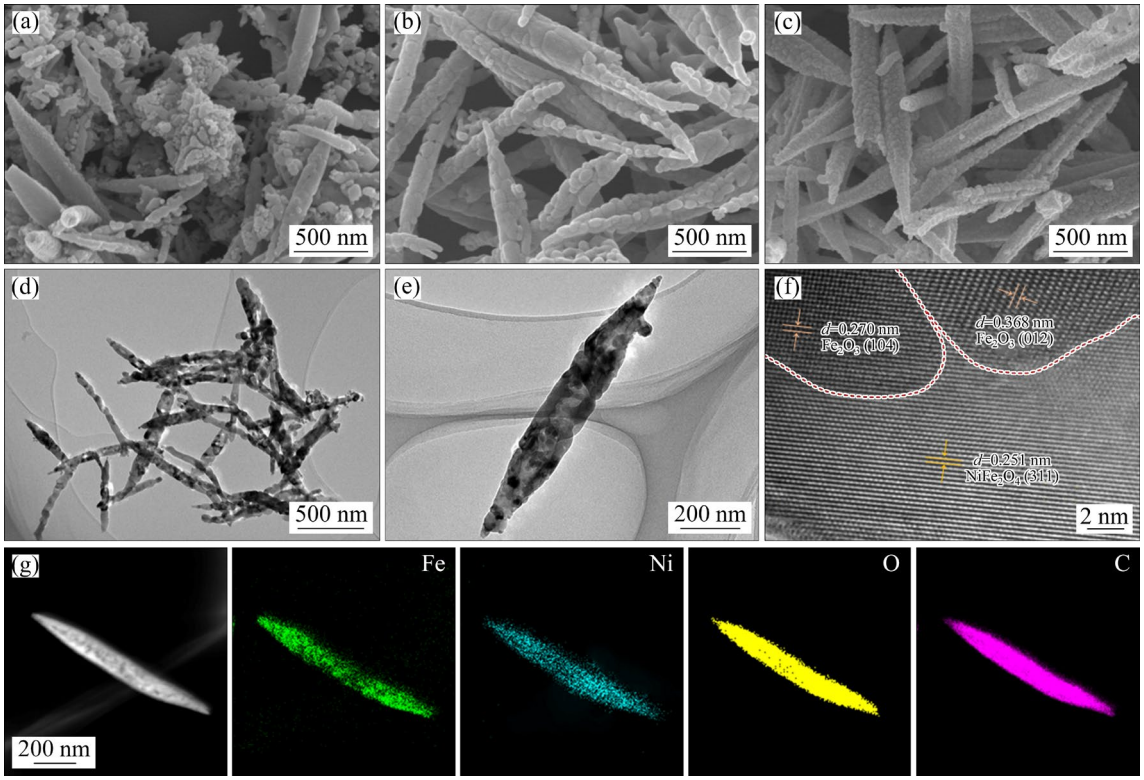

Fig. 4 SEM images of NFO/FO-0 (a), NFO/FO-6 (b) and FO-6 (c), TEM images (d, e), HRTEM image (f), and corresponding EDX mappings (g) of NFO/FO-6

potentially attributed to CO_2 produced by carbon species in the organic framework reacting with O_2 in air at high temperatures. TEM images verify the formation of porous structures in the NFO/FO-6 (Figs. 4(d) and (e)). Besides, lattice stripes with different spacings are observed in the high-resolution TEM image (Fig. 4(f)). Among them, lattice stripes with a spacing of 0.251 nm are attributed to the (311) crystal plane of $NiFe_2O_4$. In comparison, the lattice stripes with spacings of 0.270 and 0.368 nm are assigned to the (104) and (012) crystal planes of Fe_2O_3, respectively. The difference in the energy band structure of $NiFe_2O_4$ and Fe_2O_3 leads to the formation of the built-in electric field at the heterogeneous interface, which reduces the impedance and promotes electron transfer, thus enhancing the performance of LIBs [25,26]. In addition, energy dispersive X-ray spectroscopy (EDX) mapping images demonstrate the homogeneous distribution of Fe, Ni, O, and C elements throughout the NFO/FO-6 material, implying the generation of Ni and Fe-based oxides, while residual C element is caused by the incomplete pyrolysis of the organic framework in air (Fig. 4(g)).

The physical phase structures were revealed by XRD. As shown in Fig. 5(a), all materials show similar characteristic peaks and can be well-matched to the previously reported MIL-53 [21], further demonstrating the structural stability of the MIL crystal in the magnetic field. However, there are significant differences in the phase structures after pyrolysis (Fig. 5(b)). The Fe_2O_3 phase dominates in NFO/FO-0, and weak diffraction peaks of $NiFe_2O_4$ indicate its extremely small amount, while $NiFe_2O_4$ and Fe_2O_3 coexist in NFO/FO-6 with $NiFe_2O_4$ playing a dominant role. The above results illustrate that HMF increases Ni content in FeNi-MIL precursors, which may be ascribed to the homogeneous distribution of solutes caused by the MHD effect. Undoubtedly, only the Fe_2O_3 phase is detected in FO-6. The specific surface area and porosity, as important parameters affecting Li^+ storage and migration rate, were evaluated through the BET measure. Figure 5(c) displays a type IV isotherm with a distinct hysteresis

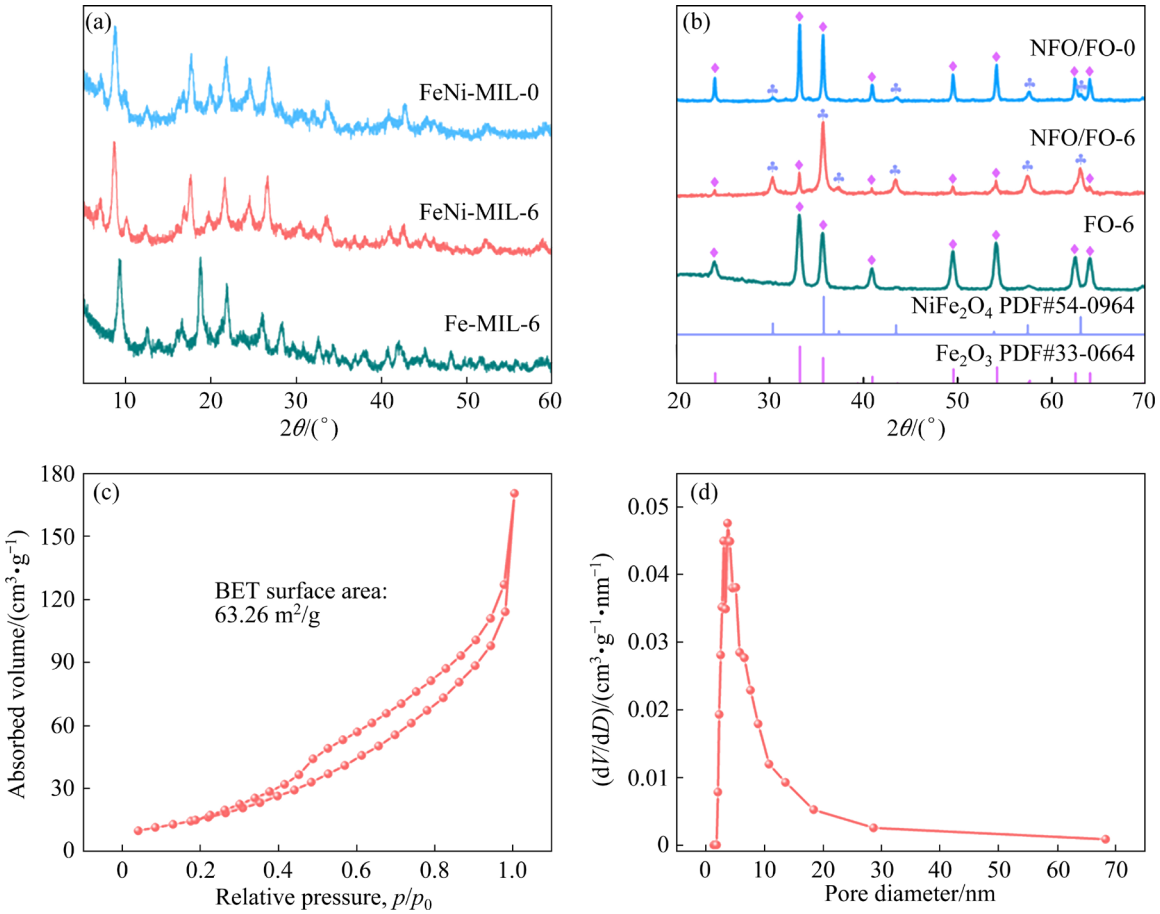

Fig. 5 XRD patterns of different precursors before (a) and after (b) pyrolysis, nitrogen adsorption and desorption isotherms (c), and pore size distribution (d) of NFO/FO-6

loop, typical of mesoporous materials, and the BET surface area is 63.26 m^2/g. Meanwhile, the pore distribution curve shows that pore diameter is in the range of 2−20 nm, which also suggests the presence of abundant mesopores in NFO/FO-6 (Fig. 5(d)). The considerable specific surface area and extensive pores not only provide released space for volume expansion but also promote the diffusion and transport of Li^+ ions.

The elemental valence and chemical composition of NFO/FO-0 and NFO/FO-6 were characterized and analyzed by XPS measurement. As seen from the XPS survey spectrum (Fig. 6(a)), Fe, Ni, O, and C elements are detected in NFO/FO-0 and NFO/FO-6, and the elemental contents are demonstrated in Fig. 6(b) and Table 1. It is obvious

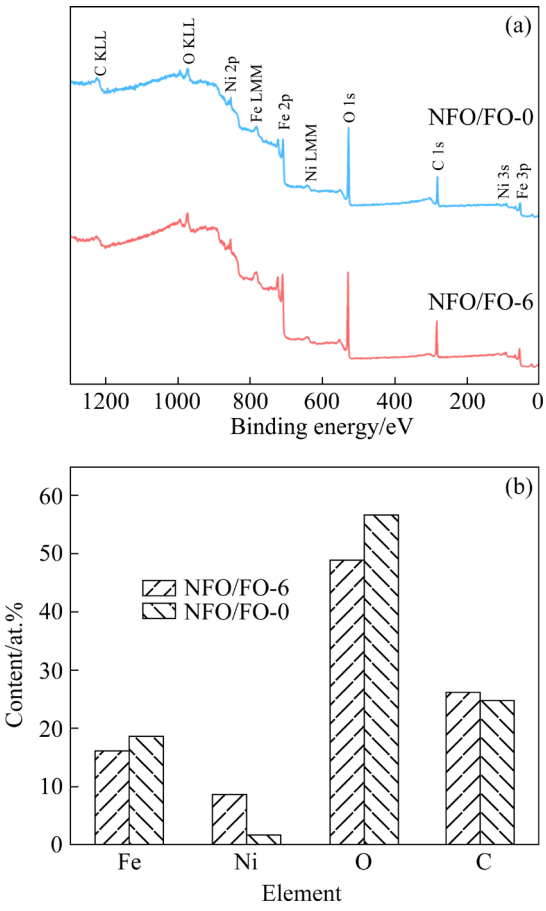

Fig. 6 XPS survey spectra (a) and element contents (b) of NFO/FO-0 and NFO/FO-6

Table 1 Element contents of NFO/FO-6 and NFO/FO-0 obtained from XPS (at.%)

Sample	Fe	Ni	O	C
NFO/FO-6	16.13	8.67	48.93	26.27
NFO/FO-0	18.69	1.78	56.70	24.83

that HMF significantly increases Ni content in NFO/FO, suggesting an increase of the $NiFe_2O_4$ spinel phase, which is consistent with the XRD results.

The high-resolution spectrum of Fe 2p shows that the two peaks at 710.6 and 725.5 eV correspond to the Fe $2p_{3/2}$ and Fe $2p_{1/2}$, respectively, and those at 718.6 and 733.1 eV to the corresponding satellite peaks (Fig. 7(a)). Interestingly, Fe^{3+} (712.2 eV) and Fe^{2+} (710.3 eV) coexist in NFO/FO, with Fe^{3+} predominating. A small amount of Fe^{2+} may be attributed to the interaction of Ni element [27]. Besides, the two prominent peaks at 855.6 and 873.1 eV in the XPS spectrum of Ni 2p (Fig. 7(b)) can be attributed to the binding energy of Ni $2p_{3/2}$ and Ni $2p_{1/2}$ with two satellite peaks around 862.3 and 879.7 eV, respectively [28]. It is worth mentioning that the appearance of partially trivalent Ni in NFO/FO-6 implies the indubitable electron transfer between Fe and Ni ions in the spinel $NiFe_2O_4$. Then, the high-resolution spectrum of O 1s (Fig. 7(c)) can be resolved into two peaks, respectively corresponding to metal−oxygen bond (M—O, 530.1 eV) and adsorbed oxygen species on the surface (531.6 eV) [29]. Noteworthy, compared with NFO/FO-0, there is a positive shift of approximately 0.3 eV toward high binding energy after imposing HMF, indicating lower electron densities of O species resulting from the electron-absorbing effect of Fe and Ni. Besides, as shown in Fig. 7(d), there are three peaks respectively belonging to C—C/C═C, C—O, and C═O at 284.8, 285.4, and 288.7 eV, attributed to the residual of carbon species in the pyrolysis process of FeNi-MIL, which enhance the electrical conductivity of NFO/FO [30].

3.3 Electrochemical performance

Given the transformation in morphology and phase structure, electrochemical properties were investigated to reveal the indirect effects of HMF on LIBs. Initially, the CV curve of NFO/FO-6 shows a slight broad reduction peak at 1.71 V in the first cathodic sweep (Fig. 8(a)), which is attributed to the insertion of Li^+ ions into Fe_2O_3 and results in the formation of $Li_xFe_2O_3$ [31]. Then, a distinct cathodic peak at 0.49 V implies the formation of solid electrolyte interfacial (SEI) film due to the interaction of Li^+ ions with organic electrolytes. The SEI film has excellent characteristics of electronic

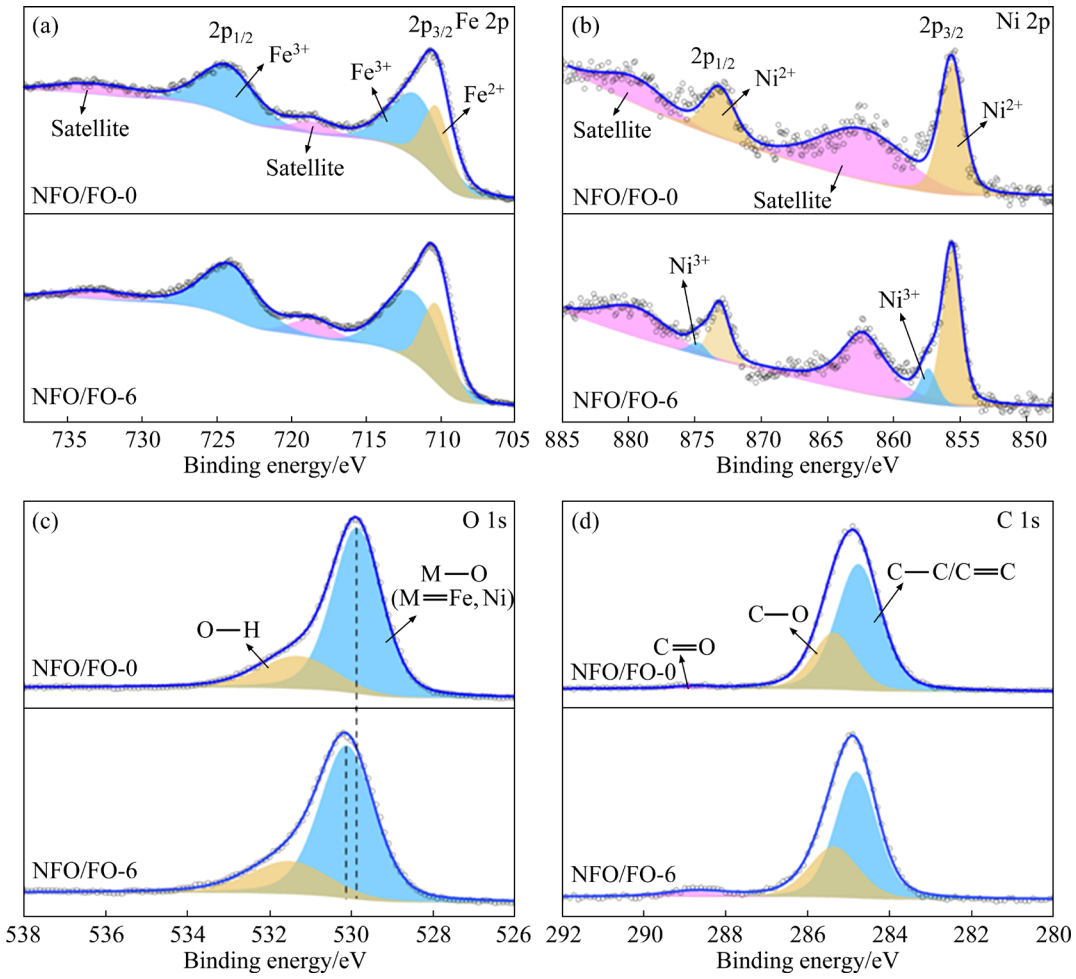

Fig. 7 High-resolution XPS spectra of NFO/FO-0 and NFO/FO-6: (a) Fe 2p; (b) Ni 2p; (c) O 1s; (d) C 1s

insulation and Li^+ ion conductivity, effectively preventing the electrolyte from damaging the electrode and improving cycle stability [32]. Notably, the irreversible peak disappears, implying that the irreversible reaction only occurs in the first cathodic sweep (Reaction (1)). Instead, a reversible cathodic peak appears at 0.78 V in the subsequent cycle, attributed to the reduction of Ni^{2+}/Ni^{3+} and Fe^{3+}/Fe^{2+} to their metallic states (Ni^0 and Fe^0). Relatively, the peak at 1.78 V can be ascribed to the reversible oxidation of metallic Fe^0 and Ni^0 to Fe^{3+} and Ni^{2+} (Reactions (2) and (3), respectively) in the anodic scanning process. The CV curves completely overlap in the second to the sixth cycles, revealing excellent electrochemical reversibility, which is fundamental for long-term cycling stability.

$$NiFe_2O_4+8Li^++8e=Ni+2Fe+4Li_2O \quad (1)$$

$$2Fe+3Li_2O\rightleftharpoons Fe_2O_3+6Li^++6e \quad (2)$$

$$Ni+Li_2O\rightleftharpoons NiO+2Li^++2e \quad (3)$$

In addition, the galvanostatic charge−discharge curves of NFO/FO-6 at 0.05 A/g show that the initial discharge and charge capacities are 1200 and 1027 mA·h/g, respectively, with a coulombic efficiency of 85.6% (Fig. 8(b)). The large irreversible capacity loss suggests the formation of SEI membranes, accompanied by irreversible reactions, which corresponds to the first CV cycle. Moreover, the discharge plateau at ~1 V and the charging plateau at ~1.8 V are attributed to the reduction and reoxidation of Fe^{3+} and Ni^{2+}, respectively. The coulomic efficiency is nearly 100% in subsequent charging−discharging, indicating good reaction reversibility. Furthermore, the first charge−discharge curves show an increase of 16% in charge−discharge capacity under the effect of HMF (Fig. 8(c)), suggesting that homogeneous morphology and phase transformation contribute to enhanced lithium storage performance. Meanwhile, 1.53-times capacity enhancement relative to FO-6 indicates that the built-in electric field between the

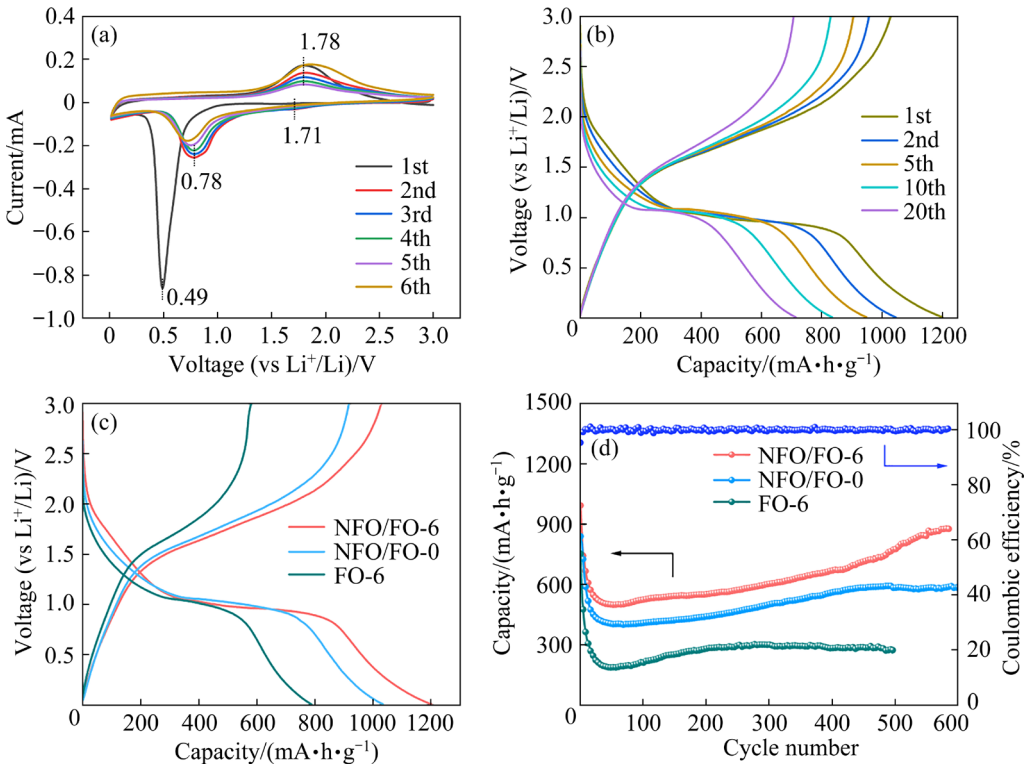

Fig. 8 CV curves of NFO/FO-6 at scan rate of 0.1 mV/s (a), galvanostatic charge−discharge curves of NFO/FO-6 at 0.05 A/g (b), and initial charge−discharge curves at 0.05 A/g (c) and cycling performance at 0.1 A/g (d) of NFO/FO-6, NFO/FO-0 and FO-6

heterogeneous interfaces of $NiFe_2O_4$ and Fe_2O_3 is more conducive to accelerating the charge transfer kinetics of Li^+ and facilitating the transport of electrons and ions.

Cycling stability was investigated as an important parameter for assessing the working life of LIBs. As shown in Fig. 8(d), the reversible capacities of NFO/FO-6, NFO/FO-0, and FO-6 respectively maintain at 876, 587, and 275 mA·h/g after 600 cycles at a current density of 0.1 A/g, with a capacity retention rate of 97.1%, 78.6%, and 44.2%, respectively. The high capacity retention can be credited to favorable Li^+ intercalation and electrolyte diffusion in active phases of the spinel $NiFe_2O_4$. Interestingly, the capacity decreases significantly in the first 20 cycles and gradually rebounds in the subsequent cycling process. This phenomenon is commonly found in metal oxide anodes, which is widely recognized as the generation of polymeric gel-like film caused by electrolyte degradation and the excess capacities supplied by pseudo-capacity after long-time cycles [33,34]. Furthermore, the structural stability of NFO/FO-6 after cycling was also clarified by SEM images. As shown in Fig. 9, NFO/FO-6 does not undergo any significant rupture or smashing, whose "shuttle" structure basically remains unchanged after 20 cycles at a current density of 0.5 A/g. The solid and stable structure ensures the high capacity retention of NFO/FO-6 during the long cycle process.

The rate properties of various materials are shown in Fig. 10(a), which are used to evaluate the performance of LIBs in different application scenarios. NFO/FO-6 exhibits the reversible capacity of 795, 670, 603, 537, and 461 mA·h/g at the current density of 0.05, 0.2, 0.5, 1, and 2 A/g, respectively. The capacity of NFO/FO-6 is consistently higher than that of NFO/FO-0 and FO-6 at the corresponding current densities. Importantly, the capacity can be recovered to 753 mA·h/g when the current density decreases to 0.05 A/g, demonstrating the recoverability of the battery capacity after high power consumption. Subsequently, the reaction kinetics of different materials was investigated by electrochemical impedance spectroscopy (EIS, Fig. 10(b)). Among them, interfacial charge transfer resistance (R_{ct}) is

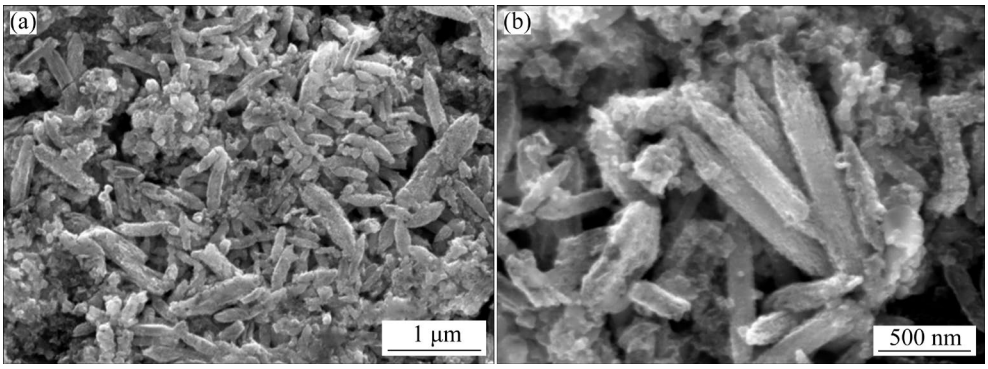

Fig. 9 SEM images of NFO/FO-6 after 20 cycles at current density of 0.5 A/g

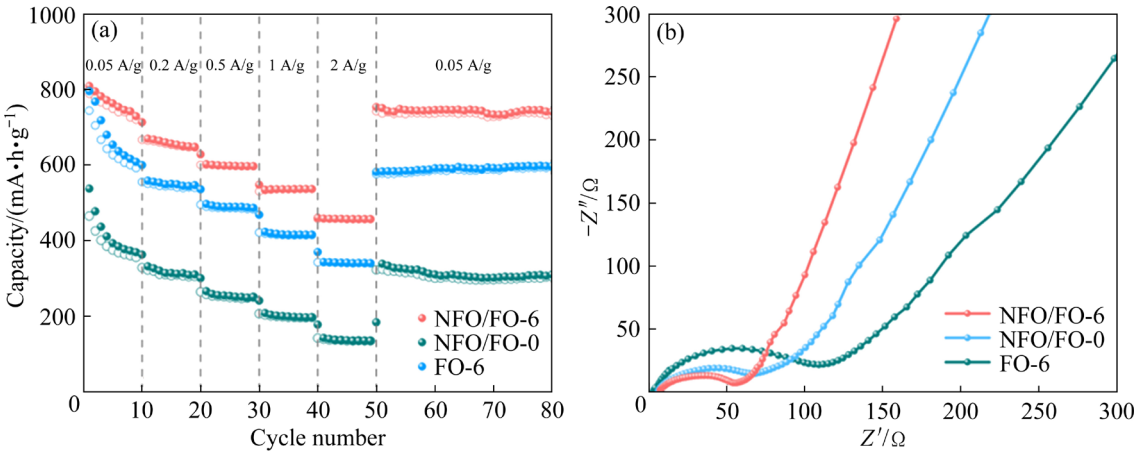

Fig. 10 Rate capability (a) and Nyquist plots (b) of NFO/FO-6, NFO/FO-0 and FO-6

considered an important parameter for assessing the electrochemical reaction rate, which is related to the semicircle of the high-frequency region. Obviously, the R_{ct} of NFO/FO-6 (54 Ω) is lower than that of NFO/FO-0 (69 Ω) and FO-6 (110 Ω), suggesting that the built-in electric field between $NiFe_2O_4$ and Fe_2O_3 heterogeneous interfaces can effectively facilitate the electron transport. Furthermore, the straight line in the low-frequency region is related to the diffusion of Li^+ ions, and the diffusion coefficient (D) can be calculated by Eqs. (4) and (5). The D values of NFO/FO-6, NFO/FO-0, and FO-6 can be identified as 1.2×10^{-14}, 2.3×10^{-15}, and 1.0×10^{-15} cm^2/s, respectively. The high Li^+ ion diffusion speed endows NFO/FO-6 with excellent charge and discharge performance at high current density.

$$D=\frac{R^2T^2}{2A^2n^4F^4C^2\sigma^2} \tag{4}$$

$$Z'=R_e+R_{ct}+\sigma\omega^{-1/2} \tag{5}$$

where R is the molar gas constant (8.314 J/(mol·K)), T is the thermodynamic temperature (K), A is the effective area of electrode (cm^2), n is the number of electrons transferred, F is the Faraday constant (96485 C/mol), C is the Li^+ ion concentration (mol/cm^3), σ is the Warburg factor (Ω·cm^2/mol), Z' is the resistance (Ω), R_e is the solution resistance (Ω), and ω is the angular frequency (rad/s).

To gain insight into the kinetic behavior of Li^+ ions, CV curves were investigated at different scan rates. The slight shift of anodic and cathodic peaks with the scan accelerating is caused by the resistance and polarization at high scan rates (Fig. 11(a)). Then, the b (b is the slope of the linear curve in Fig.11(b)) value is usually used to reveal the charge storage mechanism, which can be derived by fitting Eq. (6). b=1 indicates the surface-controlled pseudo-capacitive process, while b=0.5 indicates the diffusion-controlled faradaic behavior [35]. As shown in Fig. 11(b), the b values of cathodic and anodic peaks are 0.67 and 0.56, respectively, suggesting that diffusion combined with capacitive behaviors dedicates the charge storage of NFO/FO-6. The contribution proportion

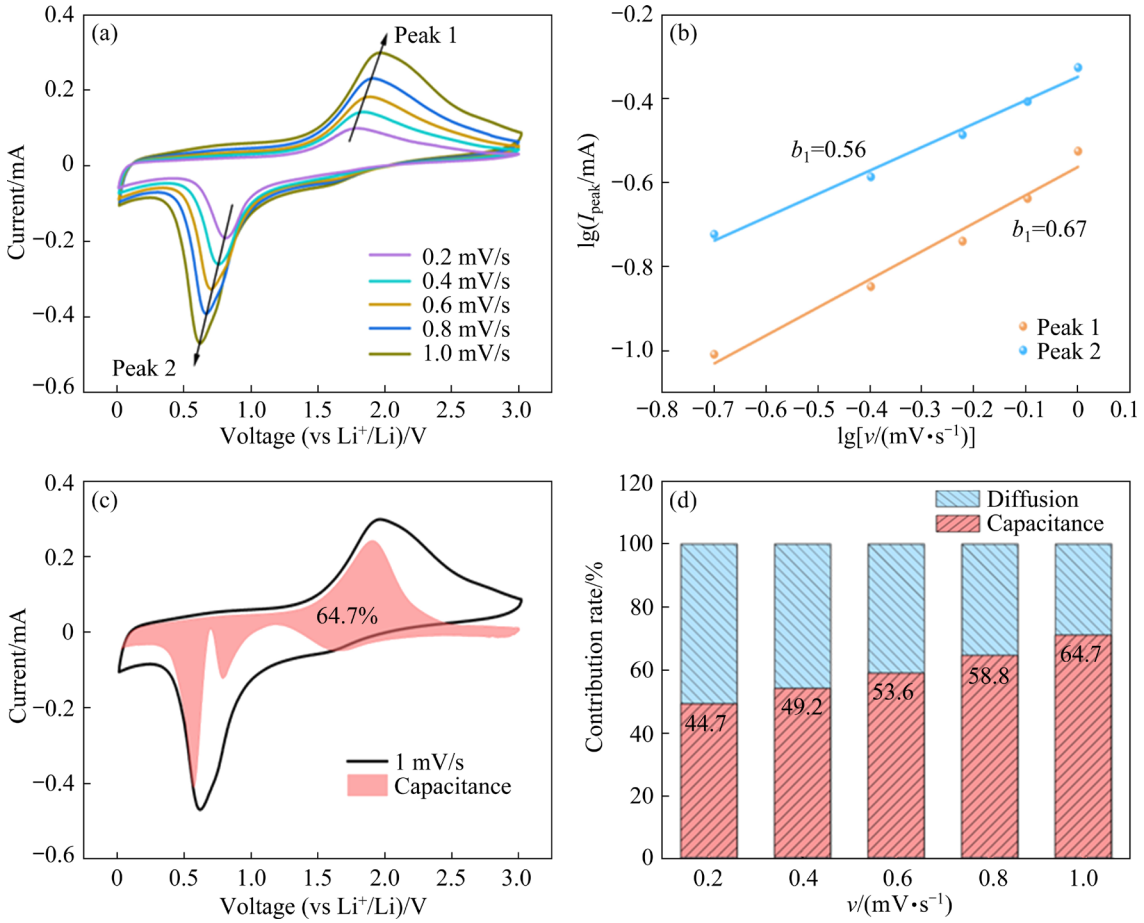

Fig. 11 (a) CV curves at different scan rates; (b) Relationship between peak current and scan rate; (c) CV curve and capacitance contribution at 1 mV/s; (d) Contribution rates of capacitance and diffusion at different scan rates

of specific capacitance can be calculated from Eq. (7). Figure 11(c) shows the CV curve at a scan rate of 1 mV/s and the corresponding capacitance contribution (shaded area). The capacitance contribution is 64.7%, signifying the dominance of capacitance in the charge storage process at 1 mV/s. The capacitance contribution decreases to 58.8%, 53.6%, 49.2%, and 44.7% as scan rate is reduced to 0.8, 0.6, 0.4, and 0.2 mV/s, respectively (Fig. 11(d)). This result demonstrates the conversion of charge storage mechanism from diffusion-dominated to capacitance-dominated, which can be attributed to the restricted Faraday behavior at large scan rates. It should be noted that the electrochemical reaction kinetics controlled by diffusive and capacitive behavior also serves as the reason for high capacity and excellent rate capability of NFO/FO-6. Specifically, the diffusion-dominated Faraday process enhances the utilization of NFO/FO-6, while the capacitance-dominated electrochemical reaction accelerates charge transfer kinetics, resulting in a high rate performance [36].

$$\lg I = b\lg v + \lg a \quad (6)$$

$$I = k_1 v + k_2 v^{1/2} \quad (7)$$

where I is the current (mA), v is the scan rate (mV/s), a is the intercept of the linear curve in Fig. 11(b), k_1 is the pseudo-capacitance contribution factor, and k_2 is the diffusion control factor.

4 Conclusions

(1) An advanced magnetic field-assisted synthesis strategy is proposed to regulate $NiFe_2O_4$/Fe_2O_3 (NFO/FO) heterogeneous structures.

(2) The MHD effect and the Seeman energy induce NFO/FO with a more homogeneous morphology and dominant phase transition from Fe_2O_3 to $NiFe_2O_4$.

(3) The increased spinel $NiFe_2O_4$ phase and built-in electric field at heterogeneous interfaces endow NFO/FO with richer active sites, faster electron transfer and higher diffusion rate of Li^+ ions.

(4) NFO/FO obtained under HMF exhibits enhanced lithium storage performance.

CRediT authorship contribution statement

Jia-qi LIU: Methodology, Data curation, Writing − Original draft; **Rong-yuan ZHANG:** Formal analysis; **Xiao-yang WANG:** Investigation, Data curation; **Jun WANG:** Project administration; **Tie LIU:** Methodology, Writing − Review & editing; **Wei-bin CUI:** Writing − Review & editing; **Qiang WANG:** Supervision; **Shuang YUAN:** Conceptualization, Supervision, Project administration.

Declaration of competing interest

The authors declare that they have no known competing financial interests or personal relationships that could have appeared to influence the work reported in this paper.

Acknowledgments

This work was supported by the National Natural Science Foundation of China (No. 52274294), the Fundamental Research Funds for the Central Universities, China (No. N2124007-1), and the Fund of the State Key Laboratory of Solidification Processing in Northwestern Polytechnical University, China (No. SKLSP202101).

References

[1] BAUER C, BURKHARDT S, DASGUPTA N P, ELLINGSEN L A W, GAINES L L, HAO Han, HISCHIER R, HU Liang-bing, HUANG Yun-hui, JANEK J, LIANG Cheng-du, LI Hong, LI Ju, LI Yang-xing, LU Yi-chun, LUO Wei, NAZAR L F, OLIVETTI E A, PETERS J F, RUPP J L M, WEIL M, WHITACRE J F, XU Sheng-ming. Charging sustainable batteries [J]. Nature Sustainability, 2022, 5(3): 176−178.

[2] GE Shan-hai, LENG Yong-jun, LIU Teng, LONGCHAMPS R S, YANG Xiao-guang, GAO Yue, WANG Dai-wei, WANG Dong-hai, WANG Chao-yang. A new approach to both high safety and high performance of lithium-ion batteries [J]. Science Advances, 2020, 6(9): eaay7633.

[3] SHEN Ya-bin, WANG Li-cheng, JIANG Ji-zhou, WANG Duo, ZHANG Dong-yu, YIN Dong-ming, WANG Li-min, ZHANG Xiu-yun, HUANG Gang, CHENG Yong. Stabilization of high-voltage layered oxide cathode by multi-electron rare earth oxide [J]. Chemical Engineering Journal, 2023, 454: 140249.

[4] YUAN Shuang, DUAN Xiao, LIU Jia-qi, YE Yun, LV Fu-sen, LIU Tie, WANG Qiang, ZHANG Xin-bo. Recent progress on transition metal oxides as advanced materials for energy conversion and storage [J]. Energy Storage Materials, 2021, 42: 317−369.

[5] WAN Li-ming, XIA Qiu-ying, WU Jiang-hua, LIU Jing, SHI Zheng-yi, LAN Si, ZHAI Teng, SAVILOV S V, ALDOSHIN S M, XIA Hui. Stabilizing charge storage of Fe_2O_3-based electrode via phosphate ion functionalization for long cycling life [J]. Rare Metals, 2023, 42: 39−46.

[6] LI Yu, ZHANG Jia-wei, CHEN Qing-guo, XIA Xin-hui, CHEN Ming-hua. Emerging of heterostructure materials in energy storage: A review [J]. Advanced Materials, 2021, 33(27): 2100855.

[7] DANG Chang-wei, YUN Si-ning, ZHANG Yong-wei, DANG Jiao-e, WANG Yin-hao, LIU Zhuo-lei, DENG Ying-ying, YANG Guang-ping, YANG Jing-jing. A tailored interface engineering strategy designed to enhance the electrocatalytic activity of $NiFe_2O_4$/NiTe heterogeneous structure for advanced energy conversion applications [J]. Materials Today Nano, 2022, 20: 100242.

[8] TANG Jian, XU Ji-lin, LI Liang-liang, MA Yong-cun, YE Zhi-guo, LUO Hong-yu, LUO Jun-ming. In-situ hydrothermal synthesis of Ni−MoO_2 heterostructure on porous bulk NiMo alloy for efficient hydrogen evolution reaction [J]. Transactions of Nonferrous Metals Society of China, 2022, 32(5): 1598−1608.

[9] ZHOU Wen-xuan, TANG Yi-jian, ZHANG Xin-yu, ZHANG Song-tao, XUE Huai-guo, PANG Huan. MOF derived metal oxide composites and their applications in energy storage [J]. Coordination Chemistry Reviews, 2023, 477: 214949.

[10] DE VILLENOISY T, ZHENG Xiao-ran, WONG V, MOFARAH S S, ARANDIYAN H, YAMAUCHI Y, KOSHY P, SORRELL C C. Principles of design and synthesis of metal derivatives from MOFs [J]. Advanced Materials, 2023, 35(24): e2210166.

[11] LV Xiu-liang, SULLIVAN P, FENG Da-wei. MOFs the movie: Molecule to nuclei evolution during metal−organic framework formation [J]. Matter, 2022, 5(1): 11−13.

[12] van VLEET M J, WENG Ting-ting, LI Xin-yi, SCHMIDT J R. In situ, time-resolved, and mechanistic studies of metal−organic framework nucleation and growth [J]. Chemical Reviews, 2018, 118(7): 3681−3721.

[13] WANG Xiao-gang, CHENG Qian, YU Yun, ZHANG Xian-zheng. Controlled nucleation and controlled growth for size predicable synthesis of nanoscale metal-organic frameworks (MOFs): A general and scalable approach [J]. Angewandte Chemie: International Edition, 2018, 57(26): 7836−7840.

[14] SHEN Kang, XU Xi-jun, TANG Yi-ping. Recent progress of magnetic field application in lithium-based batteries [J]. Nano Energy, 2022, 92: 106703.

[15] LUO Song-zhu, ELOUARZAKI K, XU Zhi-chuan. Electrochemistry in magnetic fields [J]. Angewandte Chemie: International Edition, 2022, 61(27): e202203564.

[16] WANG Zhong, YUAN Shuang, ZANG Tuo, LI Teng-xiao, ZHOU Yu-di, LIU Jia-qi, LIU Tie, WANG Kai, WANG Qiang. Preparation of a Pt−Ni_2P/NF catalyst for highly efficient hydrogen evolution using a magnetic field to promote Ni−Pt galvanic replacement [J]. Journal of Materials

Science & Technology, 2023, 142: 144−151.

[17] DING Wei, HU Lin, DAI Jian-ming, TANG Xian-wu, WEI Ren-huai, SHENG Zhi-gao, LIANG Chang-hao, SHAO Ding-fu, SONG Wen-hai, LIU Qian-nan, CHEN Ming-zhe, ZHU Xiao-guang, CHOU Shu-lei, ZHU Xue-bin, CHEN Qian-wang, SUN Yu-ping, DOU Shi-xue. Highly ambient-stable 1T-MoS_2 and 1T-WS_2 by hydrothermal synthesis under high magnetic fields [J]. ACS Nano, 2019, 13(2): 1694−1702.

[18] WAN Li, SONG Hong-yuan, CHEN Xiao, ZHANG Yu, YUE Qin, PAN Pan-pan, SU Jia-can, ELZATAHRY A A, DENG Yong-hui. A magnetic-field guided interface coassembly approach to magnetic mesoporous silica nanochains for osteoclast-targeted inhibition and heterogeneous nanocatalysis [J]. Advanced Materials, 2018, 30(25): e1707515.

[19] CHEN Hao-yun, YUAN Xing-zhong, JIANG Long-bo, WANG Hou, YU Han-bo, WANG Xin-xin. Intramolecular modulation of iron-based metal organic framework with energy level adjusting for efficient photocatalytic activity [J]. Applied Catalysis B: Environmental, 2022, 302: 120823.

[20] WANG Zhong, YUAN Shuang, LIU Jia-qi, ZHANG Yin, LIU Chen, LIU Tie, WANG Qiang. Preparation of Ni_2P nanochains with controllable geometry for the hydrogen evolution reaction by application of a high magnetic field [J]. Scripta Materialia, 2022, 219: 114892.

[21] SAMSAMI S, SARRAFZADEH M H, AHMADI A. Surface modification of thin-film nanocomposite forward osmosis membrane with super-hydrophilic MIL-53 (Al) for doxycycline removal as an emerging contaminant and membrane antifouling property enhancement [J]. Chemical Engineering Journal, 2022, 431: 133469.

[22] YANG Tao-yu, YU De-you, WANG Dong, YANG Tao, LI Ze-xiong, WU Ming-hua, PETRU M, CRITTENDEN J. Accelerating Fe(III)/Fe(II) cycle via Fe(II) substitution for enhancing Fenton-like performance of Fe-MOFs [J]. Applied Catalysis B: Environmental, 2021, 286: 119859.

[23] ZHANG Ying, ZHOU Jia-bin, CHEN Jun-hui, FENG Xiao-qiong, CAI Wei-quan. Rapid degradation of tetracycline hydrochloride by heterogeneous photocatalysis coupling persulfate oxidation with MIL-53(Fe) under visible light irradiation [J]. Journal of Hazardous Materials, 2020, 392: 122315.

[24] XIE Mao-wen, MA Yan, LIN Dun-min, XU Cheng-gang, XIE Feng-yu, ZENG Wen. Bimetal–organic framework MIL-53(Co−Fe): An efficient and robust electrocatalyst for the oxygen evolution reaction [J]. Nanoscale, 2020, 12(1): 67−71.

[25] WANG Hong-mei, WEI Yun-hong, WANG Guo-chuan, PU Yi-ran, YUAN Li, LIU Can, WANG Qian, ZHANG Yun, WU Hao. Selective nitridation crafted a high-density, carbon-free heterostructure host with built-in electric field for enhanced energy density Li−S batteries [J]. Advanced Science, 2022, 9(23): e2201823.

[26] CHEN Li, YUE Li-guo, WANG Xin-ying, WU Shang-you, WANG Wei, LU Dong-zhen, LIU Xi, ZHOU Wei-liang, LI Yun-yong. Synergistically accelerating adsorption-electrocataysis of sulfur species via interfacial built-in electric field of SnS_2-MXene Mott−Schottky heterojunction in Li−S batteries [J]. Small, 2023, 19(15): e2206462.

[27] MENG Xin, XIE Jia-hao, SUN Yu-bo, LIU Jin, LIU Bin, WANG Rong-yue, MA Fang-wei, LIU Ming-yang, ZOU Jin-long. Fe_2O_3/spinel $NiFe_2O_4$ heterojunctions in-situ wrapped by one-dimensional porous carbon nanofibers for boosting oxygen evolution/reduction reactions [J]. International Journal of Hydrogen Energy, 2022, 47(50): 21329−21343.

[28] SHEN Ya-bin, WU Ying-qiang, ZHANG Dong-yu, LIANG Yao, YIN Dong-ming, WANG Li-min, WANG Li-chen, CAO Jing-chao, CHENG Yong. Stabilization of high-voltage layered oxide cathode by utilizing residual lithium to form NASICON-type nanoscale functional coating [J]. Nano Research, 2023, 16: 5973−5982.

[29] DUAN Ran, LI Ye-jun, WANG Shu, TONG Yong-gang, RUBAHN H, ZHANG Gu-fei, QI Wei-hong. Effects of phosphate precursors on morphology and oxygen evolution reaction activity of NiFe (oxy)hydroxide on nickel foams [J]. Transactions of Nonferrous Metals Society of China, 2022, 32(12): 4050−4061.

[30] LIU Jia-qi, DANG Jie, WANG Meng, WANG Xiao-yang, DUAN Xiao, YUAN Shuang, LIU Tie, WANG Qiang. Metal-organic-framework-derived cobalt nanoparticles encapsulated in nitrogen-doped carbon nanotubes on Ni foam integrated electrode: Highly electroactive and durable catalysts for overall water splitting [J]. Journal of Colloid and Interface Science, 2022, 606: 38−46.

[31] QIN Ge-tong, DING Ling, ZENG Min, ZHANG Kai-bo, ZHANG Yu-qiang, BAI Yuan, WEN Jian-wu, LI Jing. Mesoporous Fe_2O_3/N-doped graphene composite as an anode material for lithium ion batteries with greatly enhanced electrochemical performance [J]. Journal of Electroanalytical Chemistry, 2020, 866: 114176.

[32] SHEN Ya-bin, ZHANG Xiu-yun, WANG Li-cheng, ZHANG Dong-yu, BAO Di, YIN Dong-ming, WANG Li-min, CHENG Yong, HUANG Gang. A universal multifunctional rare earth oxide coating to stabilize high-voltage lithium layered oxide cathodes [J]. Energy Storage Materials, 2023, 56: 155−164.

[33] KIM H, CHOI W, YOON J, UM J H, LEE W, KIM J, CABANA J, YOON W S. Exploring anomalous charge storage in anode materials for next-generation Li rechargeable batteries [J]. Chemical Reviews, 2020, 120(14): 6934−6976.

[34] CHOI Y S, CHOI W, YOON W S, KIM J M. Unveiling the genesis and effectiveness of negative fading in nanostructured iron oxide anode materials for lithium-ion batteries [J]. ACS Nano, 2022, 16(1): 631−642.

[35] MA Bei-bei, CHEN Shui-jiao, HUANG Ye-wei, NIE Zhen-zhen, QIU Xiao-bin, XIE Xiu-qiang, WU Zhen-yu. Electrochemical lithium storage performance of three-dimensional foam-like biocarbon/MoS_2 composites [J]. Transactions of Nonferrous Metals Society of China, 2021,

31(1): 255−264.

[36] YANG Jian, LIU Zhi-gang, SHENG Xiao-xue, LI Jia-bao, WANG Tian-yi, WANG Cheng-yin. Tin nanoparticle in-situ decorated on nitrogen-deficient carbon nitride with excellent sodium storage performance [J]. Journal of Colloid and Interface Science, 2022, 624: 40−50.

强磁场诱导 $NiFe_2O_4/Fe_2O_3$ 异质结构转变增强其储锂性能

刘家岐[1]，张荣远[1]，王晓阳[1]，王 军[2]，刘 铁[3]，崔伟斌[3]，王 强[3]，袁 双[1,4,5]

1. 东北大学 冶金学院，沈阳 110819；
2. 西北工业大学 凝固技术国家重点实验室，西安 710072；
3. 东北大学 材料电磁过程研究教育部重点实验室，沈阳 110819；
4. 东北大学 多金属共生矿生态化冶金教育部重点实验室，沈阳 110819；
5. 东北大学 低碳钢铁前沿技术教育部工程研究中心，沈阳 110819

摘 要：针对传统化学合成方法调控纳米材料结构的局限性，提出一种强磁场辅助的湿化学合成法制备 $NiFe_2O_4/Fe_2O_3$ 异质结构。研究发现，这种高能物理场可使 $NiFe_2O_4/Fe_2O_3$ 的形貌更加均匀，并诱导其物相结构由 Fe_2O_3 相向 $NiFe_2O_4$ 相转变。因此，在这种磁场下获得的优化结构可显著提高 $NiFe_2O_4/Fe_2O_3$ 作为锂离子电池负极的电化学性能，表现出 1200 mA·h/g 的放电容量(提高了 16%)和长期循环稳定性(容量保持率为 97.1%，提高了 24%)。这些结果证实了强磁场辅助策略在调节材料结构和增强储锂性能的可行性。

关键词：强磁场；$NiFe_2O_4/Fe_2O_3$；异质结构；结构调控；锂离子电池负极

(Edited by Wei-ping CHEN)